











RESEARCH ARTICLE | APRIL 05 2024

High-magnification Faraday rotation imaging and analysis of X-pinch implosion dynamics



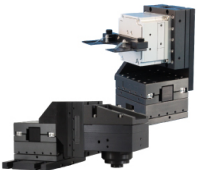
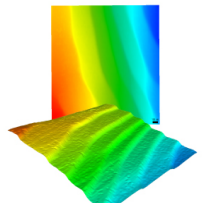
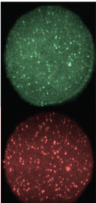
G. V. Dowhan ; A. P. Shah ; B. J. Sporer ; N. M. Jordan ; S. N. Bland ; S. V. Lebedev ; R. A. Smith ; L. Suttle ; S. A. Pikuz ; R. D. McBride 

 Check for updates

Rev. Sci. Instrum. 95, 043504 (2024)

<https://doi.org/10.1063/5.0178321>



 <p>MCL MAD CITY LABS INC. www.madcitylabs.com</p>	<p>Nanopositioning Systems</p> 	<p>Modular Motion Control</p> 	<p>AFM and NSOM Instruments</p> 	<p>Single Molecule Microscopes</p> 
--	--	--	---	--

High-magnification Faraday rotation imaging and analysis of X-pinch implosion dynamics

Cite as: Rev. Sci. Instrum. 95, 043504 (2024); doi: 10.1063/5.0178321

Submitted: 26 September 2023 • Accepted: 20 March 2024 •

Published Online: 5 April 2024



View Online



Export Citation



CrossMark

G. V. Dowhan,^{1,a)} A. P. Shah,¹ B. J. Sporer,² N. M. Jordan,² S. N. Bland,³ S. V. Lebedev,³ R. A. Smith,³ L. Suttle,³ S. A. Pikuz,⁴ and R. D. McBride^{1,2}

AFFILIATIONS

¹Applied Physics Program, University of Michigan, Ann Arbor, Michigan 48109, USA

²Nuclear Engineering and Radiological Sciences, University of Michigan, Ann Arbor, Michigan 48109, USA

³Department of Physics, Imperial College London, London SW7 2AZ, United Kingdom

⁴Lebedev Physical Institute, Russian Academy of Sciences, Moscow 119991, Russia

^{a)} Author to whom correspondence should be addressed: dowhan@umich.edu

ABSTRACT

An X-pinch load driven by an intense current pulse (>100 kA in ~100 ns) can result in the formation of a small radius, runaway compressional micro-pinch. A micro-pinch is characterized by a hot (>1 keV), current-driven (>100 kA), high-density plasma column (near solid density) with a small neck diameter (1–10 μm), a short axial extent (<1 mm), and a short duration (≲1 ns). With material pressures often well into the multi-Mbar regime, a micro-pinch plasma often radiates an intense, sub-ns burst of sub-keV to multi-keV x rays. A low-density coronal plasma immediately surrounding the dense plasma neck could potentially shunt current away from the neck and thus reduce the magnetic drive pressure applied to the neck. To study the current distribution in the coronal plasma, a Faraday rotation imaging diagnostic (1064 nm) capable of producing simultaneous high-magnification polarimetric and interferometric images has been developed for the MAIZE facility at the University of Michigan. Designed with a variable magnification (1–10×), this diagnostic achieves a spatial resolution of ~35 μm, which is useful for resolving the ~100-μm-scale coronal plasma immediately surrounding the dense core. This system has now been used on a reduced-output MAIZE (100–200 kA, 150 ns) to assess the radial distribution of drive current immediately surrounding the dense micro-pinch neck. The total current enclosed was found to increase as a function of radius, r , from a value of $\approx 50 \pm 25$ kA at $r \approx 140$ μm (at the edge of the dense neck) to a maximal value of $\approx 150 \pm 75$ kA for $r \geq 225$ μm. This corresponds to a peak magnetic drive pressure of $\approx 75 \pm 50$ kbar at $r \approx 225$ μm. The limitations of these measurements are discussed in the paper.

Published under an exclusive license by AIP Publishing. <https://doi.org/10.1063/5.0178321>

I. INTRODUCTION

In many pulsed-power-driven, high-energy-density physics (HEDP) experiments, implosions are driven via magnetic pressure generated from an axial current in a cylindrical load geometry.¹ In such a configuration, the magnetic drive pressure can be expressed as

$$P_{\text{mag}} = \frac{B^2}{2\mu_0} = \frac{\mu_0 I^2}{8\pi^2 r^2}. \quad (1)$$

Due to the I^2/r^2 dependence, very high P_{mag} can be obtained by delivering a large current, I , to a small radius, r . For example, even a modest current of only 400 kA delivered to $r = 5$ μm results in

$P_{\text{mag}} = 1$ Gbar. Additionally, the amount of P_{mag} generated can be further enhanced if a radial contraction (or implosion) occurs, since the r is further reduced.

The fact that P_{mag} increases as r decreases results in a runaway instability process called the “sausage” instability (or $m = 0$ instability, where m is the azimuthal mode number for the instability structure). This instability has been observed in a number of fast z-pinch configurations,^{2,3} including gas-puff z-pinches,⁴ wire-array z-pinches,^{5,6} and dense plasma focuses.⁷ In each case, the instability is observed in x-ray self-emission imaging as a series of discrete “bright spots” distributed randomly along the length of the background pinch column (where the background pinch column is usually about 1–2 cm long, and each bright spot has an axial extent of

only about 1 mm or less). These bright spots appear in regions where intense pinching has occurred—i.e., where the plasma column has necked down to very small radius ($\sim \mu\text{m}$). These intensely pinched regions are often referred to as “micro-pinches.”

Because of the immense magnetic pressures generated, it is desirable to study micro-pinch plasmas for HEDP applications. However, this is challenging to do because micro-pinch plasmas are physically small ($\sim \mu\text{m}$), last for very short periods of time ($\sim \text{ns}$), and appear at random locations along the length of the background pinch column. To better enable detailed studies of micro-pinch plasmas, an X-pinch configuration can be used.^{8,9} In a typical X-pinch configuration, two or more fine metal wires are crossed in the shape of an “X.” This forces the micro-pinch to form where the wires cross—i.e., where the system radius is smallest and thus the current density and magnetic pressure is highest. This allows diagnostics (particularly high-magnification imaging diagnostics) to be focused on this predetermined location in space.

The X-pinch platform has been used previously to characterize micro-pinch plasma parameters via x-ray spectroscopy.^{8,9} Studies on the 450-kA XP pulser at Cornell University have confirmed that micro-pinch plasmas are indeed in the HED regime, with electron temperatures of about 1–3 keV, ion temperatures on the order of 10 keV, and electron densities on the order of 10^{22} – 10^{23} cm^{-3} , depending on the wire material used.^{8,9} This is equivalent to material pressures ranging from 10 Mbar to >1 Gbar. Furthermore, using X-pinch-based x-ray radiography techniques, the dense cores within the micro-pinch neck-down regions have been imaged with radii as small as a few microns.^{8,9} With all 450 kA delivered to the dense core at $r = 3 \mu\text{m}$, we would have $P_{\text{mag}} > 3 \text{ Gbar}$. However, it is possible that some of the load current flows in low-density coronal plasma at radii larger than that of the dense core.^{10–12} This would reduce the magnetic drive pressure applied directly to the core. Thus, it is desirable to measure the load current’s radial distribution directly. By knowing the total current enclosed as a function of radius, $I(r)$, the radial profiles $B(r)$ and $P_{\text{mag}}(r)$ are known via Eq. (1).

To measure the load current distribution immediately surrounding a dense micro-pinch core, we have developed a Faraday rotation imaging and interferometry system. Faraday rotation diagnostics have been fielded on multiple platforms in a variety of forms.^{13–17} In general, the rotation angle is given by

$$\Delta\phi = V \int_L \mathbf{B} \cdot d\mathbf{l}, \quad (2)$$

where V is the Verdet constant, which is material and wavelength dependent. In some Faraday rotation systems, a piece of material with a large, known Verdet constant is placed at the probing location to obtain measurable rotation angles. Such systems have been successful in measuring current delivery at relatively large, cm-scale radii.^{18–20} However, due to the small size of the micro-pinch neck, it is not possible to use such a bulk material. Fortunately, though, due to the incredibly high magnetic fields in micro-pinch necks, measurable rotation angles can be obtained using only the low-density coronal plasma as the rotation medium.^{21,22}

This paper presents the design and demonstration of a high-magnification Faraday rotation imaging and interferometry diagnostic on the MAIZE pulsed power facility at the University of Michigan.^{23–25} This system has been developed specifically to measure the load current’s radial distribution in the low-density coronal

plasma surrounding the dense core of an X-pinch micro-pinch. The original goal of this diagnostic was to achieve a spatial resolution on the order of 10 μm . However, upon designing the system for practical implementation on MAIZE, the theoretical limit was estimated to be $\sim 20 \mu\text{m}$. Upon implementation, the experimental resolution turned out to be 25–35 μm (see Sec. II B 2). Though higher resolution is always desirable, the resolution achieved on MAIZE was found to be useful for resolving the spatial distributions of interest in the ~ 100 - μm -scale coronal plasma region immediately surrounding the dense micro-pinch core (see Sec. III).

II. EXPERIMENTAL SETUP AND DIAGNOSTIC DESIGN

A. MAIZE X-pinch load design

The standard crossed-wire X-pinch configuration^{8,9,27} used in these experiments is presented in Fig. 1. The design consists of anode and cathode load hardware with interchangeable CuW insert pucks. The interchangeable pucks support variations in pinch type, wire number, and crossing angle.

Experiments were run to find load configurations that were reliable and well suited for coupling with laser probing. The configuration chosen was one with two 25- μm -diameter Ag, Mo, or W wires, with a wire crossing angle $\theta_{\text{open}} = 70.6^\circ$ (see Fig. 1). This configuration gave the greatest repeatability of a clear neck region and a sharp x-ray burst (implying nominal pinching to minimal radius). The electrode pucks hold the wires 9.2 mm apart (horizontally), with an anode–cathode separation of $\sim 12 \text{ mm}$ (vertically).

The red box in Fig. 1 indicates the approximate field of view imaged by the Faraday rotation diagnostic. In the transverse direction, the field of view was between 2 mm at the highest magnification and 4 mm at the lowest magnification. Note that the camera sensor used to record the images was not square, but rather 22.2 mm wide by 14.8 mm tall. Further note that due to the timing jitter in the experimental equipment, the stochastic nature of when an X-pinch will achieve its minimum radius, and the fact that X-pinch hold their minimum radius for only $\sim 1 \text{ ns}$ or less, it is unlikely to capture an image of the pinch at its minimum radius (a few μm); rather, it is far more likely to image the pinch at a radius of 10–100 μm .

The low-impedance (0.1 Ω) MAIZE linear transformer driver (LTD) operates between 0.25 and 1 MA, with rise times of 100–300 ns, depending heavily on the inductance and resistance of

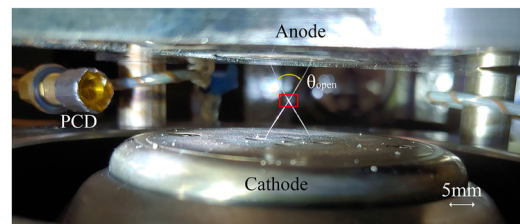


FIG. 1. *In situ* photograph within the MAIZE vacuum chamber of a standard X-pinch load with two 25- μm -diameter Ag wires and a wire crossing angle $\theta_{\text{open}} = 70.6^\circ$. Also shown are the anode and cathode orientation and the location of the diamond photoconducting detector (PCD)²⁶ used to measure the timing of the X-pinch x-ray bursts filtered for energies $> 1 \text{ keV}$. The box in red shows the approximate field of view imaged by the Faraday rotation diagnostic.

the load. During nominal operation, MAIZE delivers between 300 and 500 kA to an X-pinch load depending on the specific inductance and resistance of the geometry. However, due to machine issues, only 100–200 kA were delivered to the load during the experiments reported herein. This unfortunate circumstance led to sub-optimal magnetic fields and X-pinch dynamics for Faraday rotation imaging, but even at such low currents, the viability of the diagnostic is still demonstrated herein, with results expected to improve with restored nominal current.

B. Faraday rotation imaging

1. Theory

The Faraday effect is the rotation of polarized light while passing through a medium in the presence of a magnetic field. In a plasma, the rotation is usually well described by the quasi-longitudinal approximation^{13,28}

$$\Delta\phi = \frac{e^3\lambda^2}{8\pi^2\epsilon_0m_e^2c^3} \int_L n_e \mathbf{B} \cdot d\mathbf{l}, \quad (3)$$

where $d\mathbf{l}$ is in the direction of laser propagation. This approximation is valid as long as the electron plasma and electron cyclotron frequencies remain small compared to the laser frequency. For a 1064-nm laser, this approximation may start to break down below a radius of 15 μm for $I = 250$ kA (note that this threshold radius will increase with increasing current).

If the magnetic field and electron density profiles are azimuthally symmetric, and if the areal electron density, $N_e = \int_L n_e d\mathbf{l}$, can be measured independently of the magnetic field (e.g., from simultaneous 2D imaging interferometry), then Abel inversion allows for the extraction of the full radial magnetic field profile, $B(r)$. (Note that Abel inversion converts spatial information from the transverse projection axis, x , to the radial dimension, r .) However, if the plasma geometry deviates sufficiently from azimuthal symmetry, or if the data are particularly noisy, then Abel inversion algorithms may return noisy or nonphysical profiles. In these scenarios, alternative approximations to Abel inversion can still preserve critical information about the magnetic field and current distributions. Following Ref. 15, a simple approximation of Eq. (3) is

$$\Delta\phi \approx \frac{e^3\lambda^2}{8\pi^2\epsilon_0m_e^2c^3} N_e \bar{B}_\parallel, \quad (4)$$

where $\bar{B}_\parallel = \int_L \mathbf{B} \cdot d\mathbf{l}/L$ is the average magnetic field along (and parallel to) a ray of laser light propagating through the plasma. Inverting Eq. (4) gives^{15,28}

$$\bar{B}_\parallel \approx \frac{8\pi^2\epsilon_0m_e^2c^3}{e^3\lambda^2} \frac{\Delta\phi}{N_e} = 3.82 \times 10^{12} \frac{\Delta\phi}{\lambda^2 N_e} \text{ [SI]}. \quad (5)$$

With \bar{B}_\parallel in hand (from a measurement of $\Delta\phi$), and referring to Fig. 2, it may seem reasonable to calculate the magnetic field radial profile $B(r) = B_\theta(r) = B_y(x=r, y=0)$ using the approximation $B_y(x,0) \approx \bar{B}_\parallel(x)$. This would then allow us to calculate the enclosed current profile using

$$I_{\text{encl}}(r) = \frac{2\pi r}{\mu_0} B(r) \approx \frac{2\pi x}{\mu_0} \bar{B}_\parallel(x) \Big|_{x=r}. \quad (6)$$

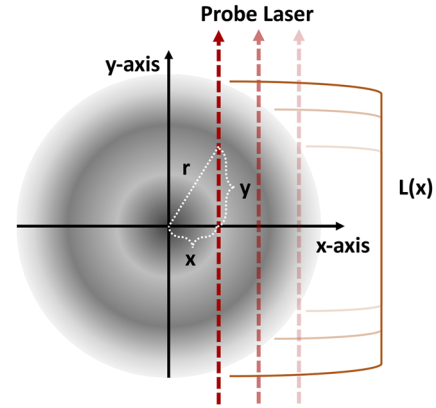


FIG. 2. A simplified slice of a cylindrical plasma with an azimuthally symmetric magnetic field profile, $B_\theta(r)$, and electron density profile, $n_e(r)$ (arbitrarily represented by the grayscale shading). The depth of the plasma for a chord of laser propagation through the plasma column changes with its position along the x -axis and is denoted as $L(x)$.

However, using this approximation results in $I_{\text{encl}}(r)$ values that are roughly half to one order of magnitude smaller than the true values. This is because $\bar{B}_\parallel(x) \leq B_y(x,0) = B(r)|_{r=x}$ for any monotonically decreasing radial profile.

To improve the approximation for $I_{\text{encl}}(r)$, the cylindrical geometry of the system can be taken into account. This can be done by first noting the geometrical relationship in the magnetic field

$$B_\parallel(x,y) = \frac{x}{\sqrt{x^2+y^2}} B(x,y), \quad (7)$$

where x is the transverse axis and y is the axis of laser propagation. Integrating Eq. (7) along a chord that cuts across the plasma column (see Fig. 2) gives

$$\begin{aligned} \bar{B}_\parallel(x) &= \frac{1}{L(x)} \int_{-L(x)/2}^{L(x)/2} B_\parallel(x,y) dy \\ &= \frac{1}{L(x)} \int_{-L(x)/2}^{L(x)/2} \frac{\mu_0 I_{\text{encl}}}{2\pi} \frac{|x|}{(x^2+y^2)} dy \\ &\approx \frac{\mu_0 \bar{I}_{\text{encl}}}{\pi L(x)} \arctan \left[\frac{L(x)}{2x} \right], \end{aligned} \quad (8)$$

where $L(x)$ is the x -dependent chord length and \bar{I}_{encl} is the mean current enclosed along the chord. For a cylindrical plasma column with an outer diameter of L_0 , we have

$$L(x) = \sqrt{L_0^2 - 4x^2}. \quad (9)$$

Substituting Eq. (9) into Eq. (8) and solving for the mean current enclosed gives

$$\bar{I}_{\text{encl}} \approx \begin{cases} \frac{\pi |\bar{B}_\parallel|}{\mu_0} \frac{\sqrt{L_0^2 - 4x^2}}{\arctan \left[\sqrt{\left(\frac{L_0}{2x}\right)^2 - 1} \right]} & \text{for } |x| < \frac{L_0}{2} \\ \frac{2\pi x}{\mu_0} \bar{B}_\parallel & \text{for } |x| \geq \frac{L_0}{2}. \end{cases} \quad (10)$$

For the regions $|x| \geq L_0/2$, we have made use of the fact that

$$\lim_{L(x) \rightarrow 0} \frac{L(x)}{\arctan\left[\frac{L(x)}{2x}\right]} = 2x. \quad (11)$$

Note that in the approximation of Eq. (10), \bar{I}_{encl} increases monotonically and nonlinearly with the selection of L_0 . Also note that for small regions of interest near the cylindrical axis, where $x \ll L_0$, the function $L(x)$ will be nearly constant. In such cases, the approximation behaves almost as a scalar multiplier, with the corrective magnitude largely determined by the choice of L_0 . The data presented in Sec. III are in this regime where $x \ll L_0$.

The error associated with applying the integral approximations of Eqs. (4), (5), and (10) is dependent on the profiles assumed for the plasma density and the enclosed current. Though the exact distributions are unknown, using reasonable trial distributions to test the effects on the results allows us to make reasonable statements about the expected uncertainty. For constant or slowly varying distributions (e.g., linear ramps), the error is typically within 10%. For more rapidly varying profiles (e.g., quadratic dependence), the error typically increases to 20%–40%. Note that for monotonic profiles, the error lessens with increasing radius. Also note that small deviations in the choice of L_0 ($\leq 10\%$) have small effects on the error ($\leq 10\%$); however, large deviations can have unpredictable effects. For the system error analysis presented in the Appendix, we use a conservative value of 30% to account for the error associated with applying the

integral approximations of Eqs. (4), (5), and (10), and a value of $\sim 8\%$ to account for the choice of L_0 .

2. System design

The basis of the diagnostic design is the Faraday rotation system fielded on the 1.4-MA, 240-ns MAGPIE generator at Imperial College London, which consists of two polarimetry channels and a simultaneous interferometry channel.^{15,29} Figure 3 shows the diagnostic as fielded on MAIZE. The probing laser source was an Ekspla NL122 Nd:YAG laser with a fundamental 1064-nm output of up to 300 mJ, a frequency-doubled 532-nm beam (125 mJ), and a frequency-tripled 355-nm beam (80 mJ). The single-pulse output has a duration of 2 ns with a jitter of 0.5 ns. The fundamental was chosen for the Faraday rotation probe to exploit the greater polarization rotation that can be expected, since Eq. (3) scales as λ^2 .

Although the laser is capable of supplying 300 mJ in the 1064-nm beam, the laser output was reduced to ~ 10 mJ in the 1064-nm beam because the polarization analyzers have damage thresholds requiring fluences below ~ 10 mJ/cm². All laser energies were measured using a coherent energy meter (J-50MB-LE) calibrated to within $\pm 2\%$ energy uncertainty. The average pulse-to-pulse energy fluctuation between subsequent laser pulses was $\sim \pm 1\%$.

The laser's output beam diameter is 6 mm. The beam is passed through a magnifying spatial filter consisting of a 200- μm pinhole and a 2 \times magnifying lens pair. The laser output in the fundamental is $>90\%$ linearly polarized. The expanded beam is then passed through an initial polarizer, denoted by P0 in Fig. 3. This polarizer

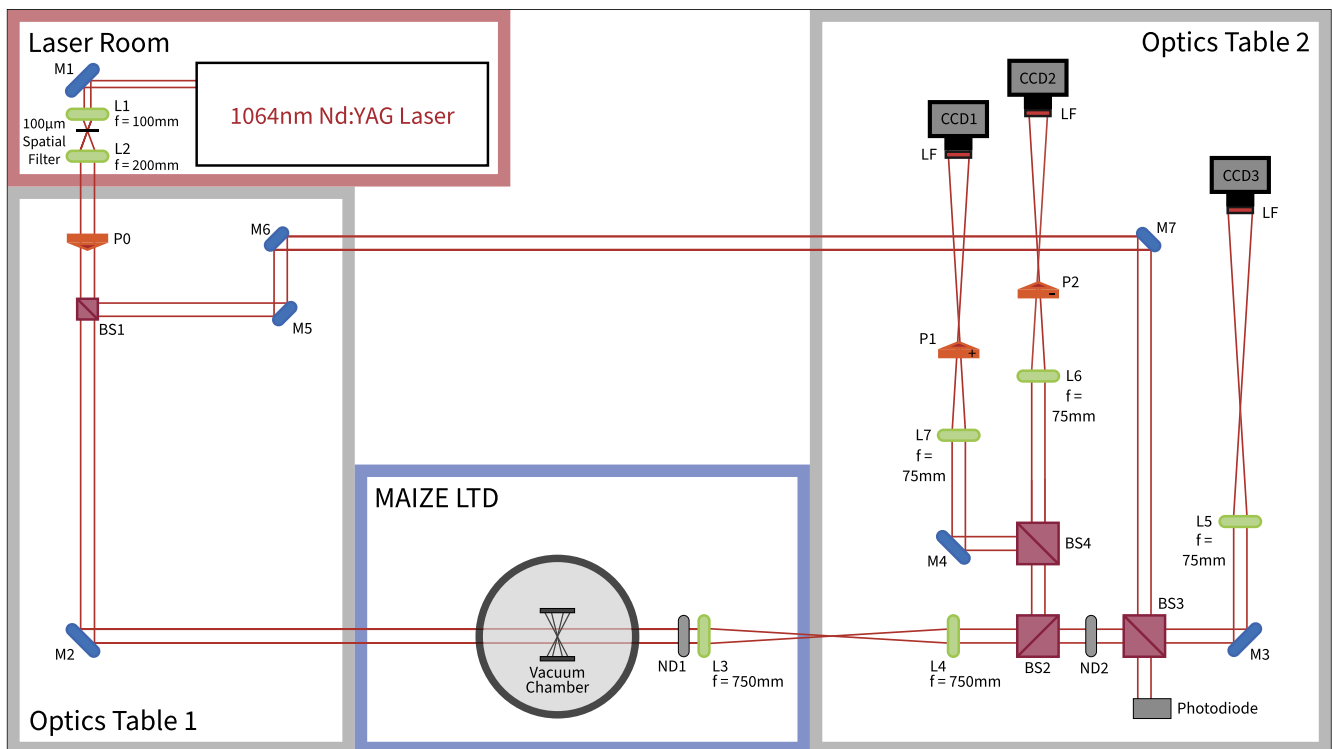


FIG. 3. Diagram of optical components and beam paths for the Faraday rotation imaging diagnostic constructed at the MAIZE facility. Diagram not to scale.

removes the vertical components (relative to the floor) and passes an almost fully horizontal polarization. The beam is then split by a 10:90 (R:T), non-polarizing beam splitter (Thorlabs BS044, denoted as BS1 in Fig. 3) into a probe beam with 90% of the incident beam energy and a reference beam with 10% of the incident beam energy. This 10:90 split is used to ensure that the probe beam has sufficient energy to be split into the Faraday and interferometry channels (beam splitters BS2, BS3, and BS4 in Fig. 3) after passing through the vacuum chamber and the X-pinch plasma.

The vacuum chamber port windows are made of an unknown material, either fused silica or Kodial glass. These windows were found to not measurably disrupt the linear polarization of the laser light. As X-pinch plasma tend to deposit material in the chamber, an additional, exchangeable/sacrificial layer of commercial borosilicate glass was used to cover/protect the port glass. Commercial borosilicate glass was used instead of Lexan panes, as Lexan panes were found to severely and nonuniformly disrupt the laser polarization.

Upon exiting the vacuum chamber, the beam and scattered light are collected by an image relay of $1\times$ magnification. For practical reasons, we placed the initial collection optic outside the 1-m-diameter vacuum chamber. This reduced the acceptance angle of the primary collection optic to 1.75° . This reduction was justifiable as sharp density gradients were expected to exist only in a very thin transition layer from the dense core plasma to the surrounding coronal plasma, and thus any loss of light from this transition region would only minimally perturb our measurement. Furthermore, a significant portion of the transition densities are likely above the laser's critical density and therefore could not be probed regardless of the acceptance angle.

The resulting numerical aperture of the system is calculated to be ~ 0.03 , corresponding to a minimum spatial resolution of $\sim 20\ \mu\text{m}$. Tests conducted with a USAF resolution target showed that features were clearly resolvable down to $35\ \mu\text{m}$, marginally resolvable down to $25\ \mu\text{m}$, and unresolvable below $25\ \mu\text{m}$ due to diffraction effects.

After being relayed, the probe beam is split three times via 50:50 (R:T) non-polarizing beam splitters (Thorlabs BS032, denoted as BS2, BS3, and BS4 in Fig. 3). The first split is such that 50% of the energy is reflected to the polarimetry channels, while the remaining 50% continues to the interferometry channel. The interferometry portion of the beam is attenuated with neutral density filters to better match the intensity of the reference beam. The attenuated probe beam and the reference beam are then recombined via BS3. The signal is then passed through a final magnifying imaging lens and collected by a 12-bit CCD camera (Canon Rebel XS with all internal filters removed). The unused portion of the recombined signal is collected by a photodiode for diagnostic timing.

The polarimetry portion of the probe beam is then split by BS4 into the two polarimetry channels, which each contain a final magnifying imaging lens and polarization analyzer (Thorlabs LPNIR100-MP2). The polarization analyzers have a high extinction ratio ($>10^7$) and a high acceptance angle ($\pm 20^\circ$). The analyzers are counter rotated to each other to $\pm\theta$ from the extinction angle. The extinction angle is determined *in situ* each time the diagnostic is assembled by mapping the full transmission profile in 1° increments. This is done to account for any background rotation introduced within the optical path. Having the two counter rotated polarimetry channels has the benefits of (1) reducing the effects of pinch self-emission and (2)

removing the double valued nature of measured rotations above θ , which is seen in systems with a paired polarimetry and shadowgraphy channel. This does come at the expense of being unable to clearly identify shadowgraphy effects. Both signals are finally collected by 14-bit CCD cameras (Canon Rebel XSi with all internal filters removed). The CCDs of both the Faraday and interferometry channels were additionally filtered with 1064-nm line filters (Edmund Optics No. 39-364, denoted as LF in Fig. 3) to reduce image contamination from broadband self-emission.

Though designed for use with X-pinch micro-pinch at high magnification, the system shown in Fig. 3 can be easily converted to low magnification operation by removing the magnification lenses and moving the CCD cameras to the image plane of the relay lenses. However, even running at $1\times$ magnification, the diagnostic is limited in probing size to a maximum of 20 mm in diameter, due to the size of the probe-reference beam splitter.

3. Simulated rotation profiles

Operation of the Faraday diagnostic at high sensitivity requires the analyzers to be rotated to the optimal offset angle based on the expected range of rotation. However, while designing this diagnostic (prior to doing any experiments), the current and density distributions surrounding the micro-pinch cores were unknown, and thus the relative magnitudes of the expected rotations were initially unknown. Therefore, simulated Faraday rotation images were generated to test the effects of various current and density distributions and to estimate the likely rotation angles.

While the overall magnetic and density profiles of X-pinch plasma are complicated and vary between experiments, a basic approximation can be made by assuming that the neck region, or any subsection of the neck region, can be described by a cylindrically symmetric region composed of a critically dense neck that sharply transitions to coronal plasma. The magnitude of the rotation angles that might be observed can then be calculated by imposing varied density and current profiles within this geometry.

Figure 4 shows a selection of rotation profiles through the parameter spaces explored. Figures 4(a)–4(c) show the effects of constant, linear, and exponential electron density profiles with the full drive current contained within the dense neck plasma. Figures 4(d)–4(f) show the effects of a constant electron density in the coronal plasma and the current now being partitioned between the dense neck and the coronal plasma with 90%, 50%, and 10% of the drive current within the neck plasma and the remaining current being linearly distributed in the surrounding coronal plasma. Each plot is normalized to a coronal electron density of $2 \times 10^{18}\ \text{cm}^{-3}$ at the edge of the neck. This value is roughly the average value of what initial interferometry results had indicated. Regardless of the exact variants considered, simulations within the range of expected parameters produced similar maximal rotation values. Taking into account self-emission effects, this provided an initial value for the analyzing polarizers of $<10^\circ$ for expected densities of $10^{18}\ \text{cm}^{-3}$ and a current of 150 kA. For the experiments reported herein, analyzer offset angles of 5° or less were found to provide the highest sensitivities, which is roughly in line with the simulated estimates. Note that the rotation angle is linear with current. Therefore, having greater current at equivalent densities would improve the signal strength and thus the signal-to-noise ratio for a given density profile.

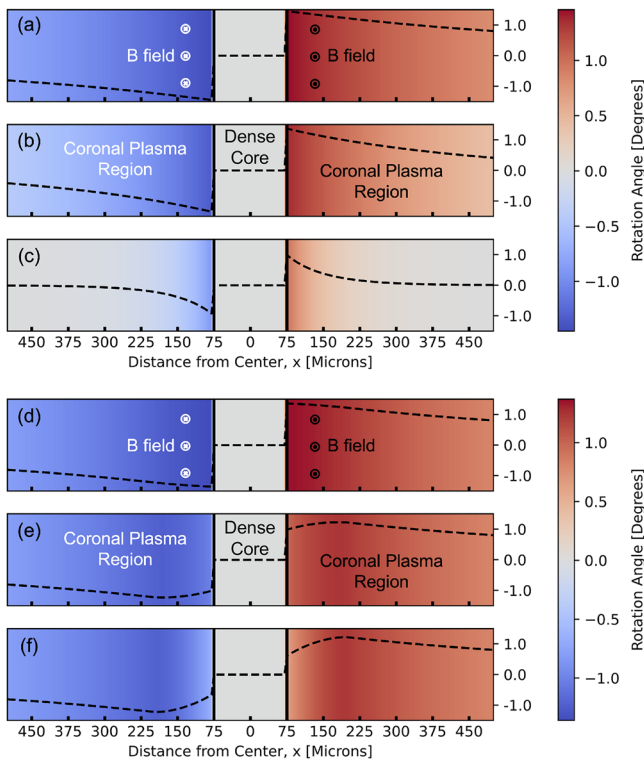


FIG. 4. (a)–(c) Simulated Faraday rotation profiles with the entire current enclosed within the central dense plasma column and (a) constant, (b) linear, and (c) exponential electron density distributions in the surrounding coronal plasma. (d)–(f) Simulated Faraday rotation profiles of a constant electron density distribution in the coronal plasma and (d) 90%, (e) 50%, and (f) 10% of the total drive current contained within the dense neck plasma and the remaining current being linearly distributed in the surrounding coronal plasma. The line out of each simulated rotation profile is plotted in black along with the location of the edges of the central dense neck plasma. All plots were normalized with a coronal plasma density of $2 \times 10^{18} \text{ cm}^{-3}$ at the edge of the neck and a total current of 150 kA.

III. EXPERIMENTAL RESULTS

For each X-pinch experiment, nine images are produced by the diagnostic: a pre-shot image, an image taken during the experiment, and a post-shot image for each of the polarimetry channels and the single interferometry channel. Figure 5 shows example interferometric images, while Fig. 6 shows the corresponding polarimetric images. For these sets of images, the analyzer angles were set to $\pm 3.5^\circ$. In general, magnifications were about 7.5–8 \times , corresponding to approximately $0.66 \mu\text{m}$ per CCD pixel. Note that these pixel resolutions are higher than the achievable optical resolution, but they are still desirable for reducing what would be an extraneous field of view on the sensor and for easing image registration and alignment when processing the images.

Figure 6(d) shows a plot of the rotation angle calculated from the box-filtered polarograms of Figs. 6(b) and 6(c), normalized to their post-shot background polarograms, one example of which is presented in Fig. 6(a). Using the post-shot background for normalization is preferred over using the pre-shot background because the

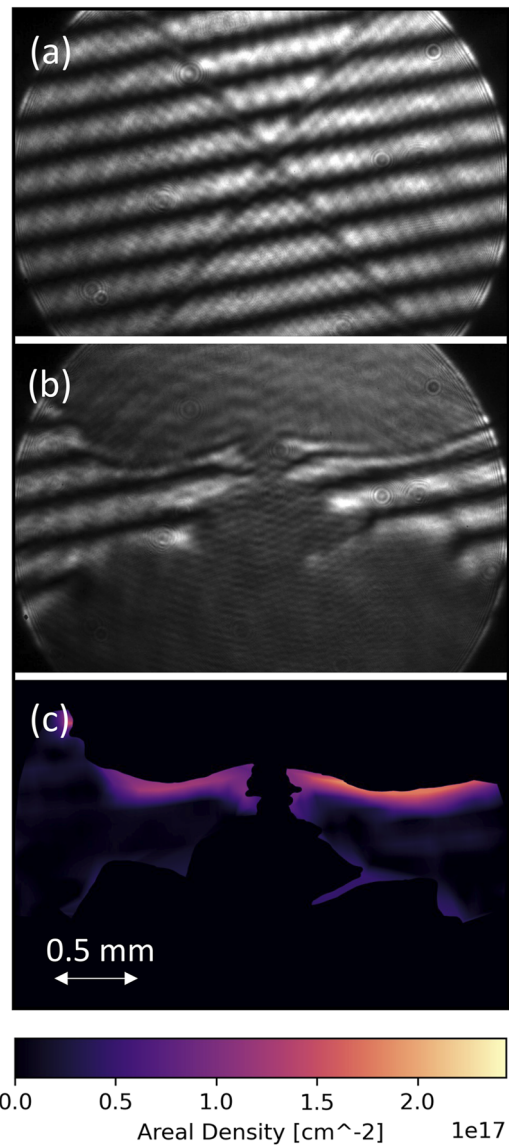


FIG. 5. Interferometry data for an example two-wire, 25- μm -wire-diameter, Ag X-pinch experiment: (a) pre-shot interferogram; (b) interferogram; (c) the areal density calculated from (a) and (b). The density range shown ($\sim 10^{16}$ – 10^{17} cm^{-2}) is typical for standard 2-wire X-pinch experiments on MAIZE.

presence of the wires in the pre-shot background leads to numerical artifacts in the region of interest. Following Ref. 15, the rotation angles were calculated from the polarograms via

$$\Delta\phi(x, y) = \frac{1}{2} \left[\frac{E_B(x, y)}{E_S(x, y)} \left\{ \frac{I_{S+}(x, y)}{I_{B+}(x, y)} - \frac{I_{S-}(x, y)}{I_{B-}(x, y)} \right\} \frac{\tan(\theta)}{2} \right], \quad (12)$$

where the subscripts “S” and “B” refer to the shot and background values of the laser energy (or image intensity), and the subscripts “+” and “–” refer to the polarimetry channels with their analyzers rotated by \pm the selected angle θ . In Fig. 6(d), the measured

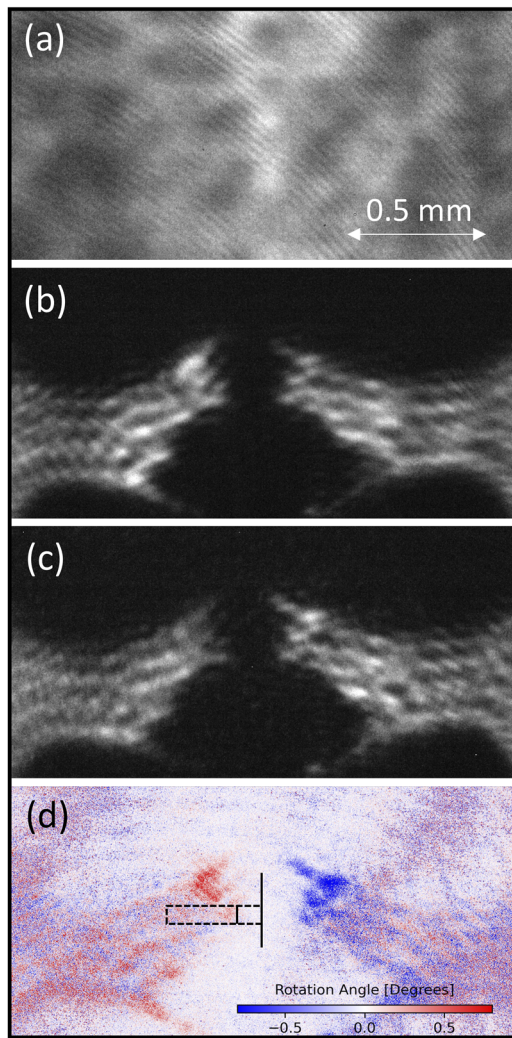


FIG. 6. Polarimetry data from the example two-wire, 25- μm -wire-diameter, Ag X-pinch experiment: (a) post-shot polarimetry background; (b) smoothed channel 1 polarogram; (c) smoothed channel 2 polarogram; and (d) the Faraday rotation image calculated from (a)–(c). The dashed box in (d) denotes the region used for producing the enclosed current profile of Fig. 7 and the magnetic pressure profile of Fig. 8. The solid lines within the dashed box in (d) denote the centerline and edge of the dense core.

angles range mainly within $\pm 1^\circ$ and were not close to exceeding $\beta = \pm 3.5^\circ$. This would not be an issue, regardless, as the dual channel polarimetry removes the double valued nature of the rotation when determined by Eq. (12). Rather, this simply indicates that the sensitivity may be slightly improved by setting the analyzers to a slightly smaller value of $|\pm \theta|$.

Note that the images in Figs. 5 and 6 appear slightly defocused. This is likely due to some combination of edge diffraction, motional blurring due to time-integration over the 2-ns laser pulse, a shallow depth-of-field, and a slight optical misalignment. Reducing the time-integration would require a new laser, while the depth-of-field could be extended in future experiments by reducing the aperture

of the collection lens. However, reducing the aperture of the collection lens would likely exacerbate the diffraction effects. Thus, in the future, coherent ray-tracing simulations should be run (and confirmatory experimental tests should be performed) to find the optimal f-number for the system. Regarding the edge diffraction apparent in the images of Fig. 6, we note that the diffraction pattern generated is influenced by the shape of the dense plasma neck at the time of the image. When using these data to extract 1D radial profiles, the diffraction pattern shows up as an oscillatory component superimposed onto a mean value. Fortunately, in regions of interest closer to the neck edge (i.e., where the rotation angle is relatively large), the amplitude of the oscillatory component is small enough relative to the mean value that we can still extract radial distributions (or at least their general trends) with reasonable quantitative accuracy.

For processing the interferograms, we made use of the Magic2 code developed at Imperial College London from the original MAGIC code.^{30,31} Essentially, this required the preprocessing of a background interferogram and an experimental interferogram with single-pixel, black fringe traces on a white background. Any unused portions of the image, such as regions blocked by dense plasma, were masked in gray. These preprocessed interferograms were loaded into the code, and the user was asked to label the fringes on both interferograms. Magic2 then interpolated between the labeled fringes and returned the resulting fringe shift map. The extracted fringe shift map was then converted to areal density [e.g., Fig. 5(c)]. Refer to the Appendix in Ref. 32 for more information on the Magic2 code and its methods.

Here, we note that processing the interferograms was excessively challenging due to a low fringe density and to large portions of the images being unusable because of the dense X-pinch plasma scattering or attenuating the probe beam. Higher fringe density would have improved the spatial resolution of the computationally determined areal density; however, the trade-off between fringe density and sensitivity would have reduced the sensitivity of the interferogram to below the noise threshold. From the interferogram of Fig. 5(b), it is seen that fringe shifts remain small until very close to the neck. This implies that much of the neck region is devoid of sufficient plasma density for measurable rotation angles, except where plumes of density exist or where the magnetic field strength becomes large enough (e.g., at small radius) to utilize the minimal density present.

For both the interferometry and polarimetry data, Abel inversion was attempted to account for the cylindrical geometry of the system. However, the low sampling density of the fringe shifts and the edge diffraction within the rotation angle profile resulted in noisy or nonphysical inverted profiles. Therefore, \bar{B}_\parallel was calculated using Eq. (5) with our measured values of $\Delta\phi$ and N_e . The sampled rotation and areal density values were first interpolated to smooth the profiles before being combined into an averaged \bar{B}_\parallel profile. The enclosed current was then calculated from Eq. (10) using an estimate of L_0 .

There are various interpretations for L_0 based on known parameters. The first is that there will be a maximal L_0 for which the extracted current trace will match the amplitude captured by the anode Rogowski coil, as it would not be possible to have greater current to the load. The second is that for any fully enclosed current surrounded by a region devoid of further current density, the magnetic pressure profile should decay as $1/r^2$, and the current enclosed

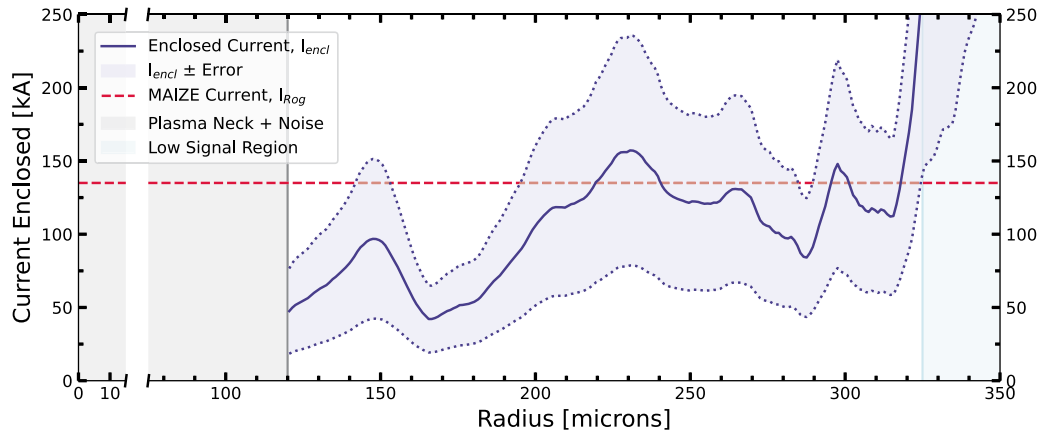


FIG. 7. Current enclosed as a function of radius from the center of the X-pinch neck calculated using a length scale of $L_0 = 2500 \mu\text{m}$. The shaded region bounded by the dotted line gives the calculated errors in the enclosed current measurement. Plotted for reference in red is the 133 kA of load current measured by the anode Rogowski coil on MAIZE at the time of the Faraday rotation imaging. Note that the anode Rogowski coil resides at a radius of 11 cm.

profile should be constant with r , even in vacuum. However, Faraday rotation imaging is not possible for probed regions containing only vacuum (or sufficiently low plasma density). The radius above which the plasma density becomes too low for a Faraday rotation signal to be obtained will result in nonsensical magnetic pressure and current enclosed values, often appearing as regions of large amplitude noise at large radius. The transition from expected radial dependence to regions of large amplitude noise often occurs abruptly at a particular radial location. Thus, we may use this transition point to specify a minimal L_0 . (Recall that L_0 is twice the radius of where this transition occurs, since in our approximation, L_0 is defined as the diameter of the plasma column.) If no transition point is visible within the radial field of view ($\sim 1500 \mu\text{m}$), then an assumption for L_0 can be made from a reasonable point of decay in the magnetic pressure curve. Alternatively, if the interferometry data show plasma density beyond the Faraday rotation imaging region of interest (as is the case

for the experiments presented herein), then the interferometry data should be used to choose L_0 based on the radial location where the density profile transitions to a rapidly decaying signal with increasing radius. This was the procedure used to determine the value of $L_0 = 2500 \mu\text{m}$ for the results presented in Figs. 7 and 8. This value for L_0 also resulted in our profile amplitudes matching the mean amplitudes obtained from much noisier and chaotic Abel inversion attempts. This agreement with Abel inverted signals (though crude) provides supporting evidence for our choice of L_0 and increases our confidence in our approximations.

Figure 7 shows the average current enclosed as a function of distance from the center of the plasma neck for the X-pinch images shown in Figs. 5 and 6, calculated using a length scale of $L_0 = 2500 \mu\text{m}$. This profile shows that the current enclosed in the dense plasma column at $r \leq 120 \mu\text{m}$ is only $\sim 40\%$ – 50% of the total load current delivered, which was $\sim 133 \text{ kA}$ at the time of imaging (as

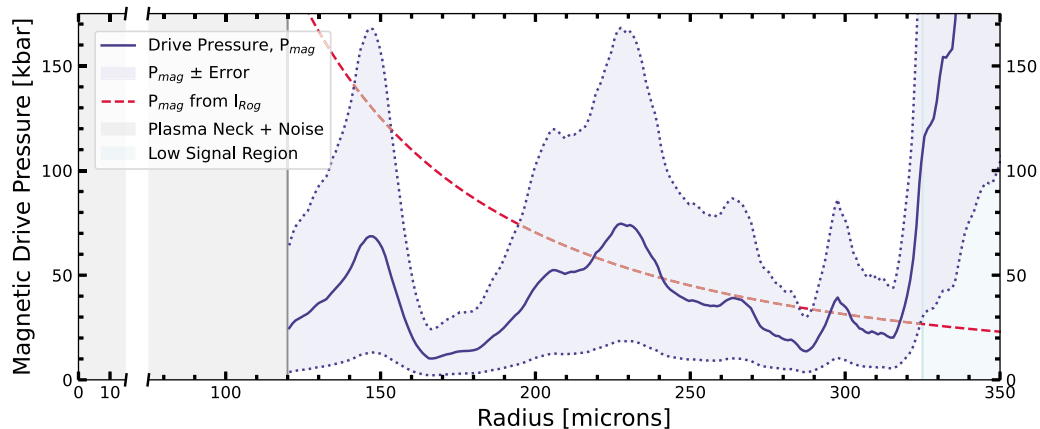


FIG. 8. Magnetic drive pressure as a function of radius from the center of the X-pinch neck calculated using a length scale of $L_0 = 2500 \mu\text{m}$. The shaded region bounded by the dotted line gives the calculated errors in the drive pressure measurement. The overlaid dashed red line shows a fit with a $1/r^2$ dependence. Note that a $1/r^2$ dependence is expected to occur outside of the radius in which 100% of the total drive current is enclosed [cf. Eq. (1)].

measured by MAIZE's anode Rogowski coil that resides at a radius of 11 cm). The enclosed current then increases to relatively constant values of approximately 85%–100% at $r > 210 \mu\text{m}$. This implies that roughly 40%–60% of the total drive current is distributed within the coronal plasma surrounding the dense core. Loss of measurement fidelity (e.g., edge diffraction effects) is the likely cause of the dip in the current enclosed trace of Fig. 7, and the increase in the current enclosed appears reasonably linear with radius if the dip is ignored. At larger distances from the neck ($r > 325 \mu\text{m}$), the inferred current enclosed takes on nonphysical values from regions with lower signal-to-noise ratios in the Faraday rotation images. This is denoted by the shaded region labeled “Low Signal Region” in Figs. 7 and 8. To improve the signal-to-noise ratios, the current enclosed profile is averaged vertically along the neck [see the region of interest within the dashed box in Fig. 6(d)]. This comes at the expense of increasing the minimal resolvable neck radius. Hence, the shaded region in Fig. 7 that is denoted as “Plasma Neck + Noise” is slightly broader than the minimal diameter seen in Figs. 5(b), 5(c), and 6(b)–6(d).

Finally, Fig. 8 shows the magnetic drive pressure radial profile that corresponds to the current enclosed profile of Fig. 7. The $P_{\text{mag}}(r)$ profile plotted in Fig. 8 was calculated using Eq. (1), with $I = I_{\text{encl}}(r)$. Due to the low drive current and large radius of measurement in this experiment, the maximum magnetic pressure measured reached only ~ 75 kbar (at a radius of about $225 \mu\text{m}$). Also plotted in Fig. 8 is the $1/r^2$ curve derived from assuming that the total current measured by the MAIZE Rogowski coil is contained within the dense plasma column. As can be seen, the curve matches the data reasonably well at radii $\geq 210 \mu\text{m}$. This is encouraging because a $1/r^2$ dependence is expected to occur outside of the radius in which 100% of the total drive current is enclosed [cf. Eq. (1)].

IV. CONCLUSIONS

A Faraday rotation imaging diagnostic has been designed and fielded on the MAIZE LTD facility with simultaneous polarimetric and interferometric imaging. The diagnostic has been fielded with magnification values ranging from 4 to $8\times$ with sufficient sensitivity to measure low areal densities ($\sim 10^{17} \text{ cm}^{-2}$) in the coronal plasma surrounding the dense micro-pinch neck. Despite low currents leading to small rotation angles of less than 2° , the diagnostic had the sensitivity required to readily detect rotation signals in this range. Having demonstrated sufficient magnification and sensitivity to both density and rotation around an X-pinch micro-pinch, the primary goal of the diagnostic to extract enclosed current profiles and magnetic drive pressure profiles has been achieved.

Experiments with higher drive currents restored on MAIZE (≥ 500 kA) will increase the diagnostic's signal-to-noise ratios, which will extend and improve the diagnostic's output; however, this may not significantly improve the minimal measurable radius. If measurements can be made down to a neck radius of $\sim 30 \mu\text{m}$ (the present system resolution), and if all of the current remains close to the dense core (within $30 \mu\text{m}$ of the neck edge), then we may be able to directly measure a magnetic drive pressure of >10 Mbar [cf. Eq. (1)].

To improve the system, a new sub-ns laser source could be acquired, as the present 2-ns laser probe limits the minimum radius

that can be measured to 50–100 μm due to temporal averaging and motional blurring. This is because the primary neck cascade (implosion) occurs in $\lesssim 2$ ns, with high convergence existing for only a fraction of that time. To reduce diffraction effects, we could use a shorter wavelength laser for the polarimetry channels, since the diffraction-limited spatial resolution scales with λ . For example, we could use the laser's 532-nm harmonic beam instead of its 1064-nm fundamental beam. This may improve the diffraction-limited spatial resolution by a factor of 2, but doing so is only useful if sufficient rotation angles can be sustained for adequate signal-to-noise ratios, since the rotation angle (our desired signal) scales with λ^2 [see Eq. (3)]. Other potential improvements include relocating the pair of image relay optics to sit fully or partially within the MAIZE vacuum chamber. This would further reduce diffraction effects while also increasing the collection angle for light refracted from steep density gradients. In turn, this would improve our ability to resolve the plasma density and magnetic field closer to the neck edge. We also note that the addition of a dedicated shadowgraphy channel could help with identifying spurious issues arising from steep density gradients. These improvements to the system, coupled with synthetic diagnostic output from advanced plasma simulations, will allow for better verification of the enclosed current and magnetic pressure distributions close to the dense core in future studies.

ACKNOWLEDGMENTS

This work was supported by the DOE Early Career Research Program under Grant No. DE-SC0020239 and by the NNSA SSAP under Cooperative Agreement Nos. DE-NA0003764 and DE-NA0004148.

AUTHOR DECLARATIONS

Conflict of Interest

The authors have no conflicts to disclose.

Author Contributions

G. V. Dowhan: Conceptualization (equal); Data curation (lead); Formal analysis (lead); Investigation (lead); Methodology (lead); Project administration (equal); Resources (equal); Software (equal); Supervision (equal); Validation (equal); Visualization (equal); Writing – original draft (equal); Writing – review & editing (equal). **A. P. Shah:** Conceptualization (supporting); Data curation (supporting); Investigation (supporting); Methodology (supporting). **B. J. Sporer:** Data curation (supporting); Investigation (supporting). **N. M. Jordan:** Project administration (supporting); Resources (supporting); Supervision (supporting). **S. N. Bland:** Conceptualization (supporting); Methodology (supporting). **S. V. Lebedev:** Conceptualization (supporting); Methodology (supporting). **R. A. Smith:** Conceptualization (supporting); Methodology (supporting). **L. Suttle:** Conceptualization (supporting); Methodology (supporting). **S. A. Pikuz:** Conceptualization (supporting); Methodology (supporting). **R. D. McBride:** Conceptualization (equal); Formal analysis (supporting); Investigation (supporting); Methodology (equal); Project administration (lead); Resources (supporting); Supervision (lead); Writing – review & editing (equal).

DATA AVAILABILITY

The data that support the findings of this study are available from the corresponding author upon reasonable request.

APPENDIX: ERROR PROCEDURE FOR ENCLOSED CURRENT AND MAGNETIC PRESSURE

The error bounds presented in Figs. 7 and 8 were derived primarily as *estimates* of the experimental error following normal error propagation in quadrature assuming fully independent error sources. From Eq. (10), the error in the enclosed current is dependent on the error in the average parallel magnetic field, $\bar{B}_{\parallel}(x)$, and the error in the transverse projection axis, x . The error in the projection axis is separated into two terms dependent on the projected axis and the length scale parameter, L_0 . The error in the enclosed current can be simplified to the form

$$\frac{\sigma_{I_{\text{encl}}}}{\bar{I}_{\text{encl}}} = \begin{cases} \sqrt{\left(\frac{\sigma_{\bar{B}_{\parallel}}}{\bar{B}_{\parallel}}\right)^2 + C_1\left(\frac{\sigma_{L_0}}{L_0}\right)^2 + C_2\left(\frac{\sigma_x}{x}\right)^2} & \text{for } |x| < \frac{L_0}{2}, \\ \sqrt{\left(\frac{\sigma_{\bar{B}_{\parallel}}}{\bar{B}_{\parallel}}\right)^2 + \left(\frac{\sigma_x}{x}\right)^2} & \text{for } |x| \geq \frac{L_0}{2}, \end{cases} \quad (\text{A1})$$

where the coefficients are defined as

$$C_1 = \left(\frac{L_0^2}{L^2} - \frac{2x}{L \arctan\left(\frac{L}{2x}\right)}\right)^2, \quad (\text{A2})$$

$$C_2 = \left(\frac{2x}{L \arctan\left(\frac{L}{2x}\right)} - \frac{4x^2}{L^2}\right)^2, \quad (\text{A3})$$

and where $L = \sqrt{L_0^2 - 4x^2}$. To include an estimate of the error associated with applying the integral approximations of Eqs. (4), (5), and (10), a conservative estimate of 30% error is then convolved with the error calculated from Eq. (A1). From Eq. (1), the error bounds of the enclosed current profiles give the error in the magnetic pressure.

The error in the radial projection axis, x , is found directly from the average of the spatial scale errors found for each image; it is a constant relative error. From Eq. (5), $\bar{B}_{\parallel}(x)$ is dependent on the areal density, N_e , and on the Faraday rotation angle, $\Delta\phi$. Thus, the error equation for $\bar{B}_{\parallel}(x)$ is

$$\frac{\sigma_{\bar{B}_{\parallel}}}{\bar{B}_{\parallel}} = \sqrt{\left(\frac{\sigma_{\Delta\phi}}{\Delta\phi}\right)^2 + \left(\frac{\sigma_{N_e}}{N_e}\right)^2}. \quad (\text{A4})$$

The error in the areal density is calculated from the uncertainties in the measurements of the fringe shifts and the fringe periods. From Eq. (12), the error in the Faraday rotation angle is a function of the laser energy ratio between the background and shot images, the error in the analyzer angle, and the error in the pixel overlap between the two polarimetry channels. The overlap error was estimated by calculating the average standard deviation from shifting the channels relative to each other in the x , y , xy , and $-xy$ directions by a set number of pixels.

REFERENCES

- ¹R. D. McBride, W. A. Stygar, M. E. Cuneo, D. B. Sinars, M. G. Mazarakis, J. J. Leckbee, M. E. Savage, B. T. Hutsel, J. D. Douglass, M. L. Kiefer, B. V. Oliver, G. R. Laity, M. R. Gomez, D. A. Yager-Elorriaga, S. G. Patel, B. M. Kovalchuk, A. A. Kim, P.-A. Gourdain, S. N. Bland, S. Portillo, S. C. Bott-Suzuki, F. N. Beg, Y. Maron, R. B. Spielman, D. V. Rose, D. R. Welch, J. C. Zier, J. W. Schumer, J. B. Greenly, A. M. Covington, A. M. Steiner, P. C. Campbell, S. M. Miller, J. M. Woolstrum, N. B. Ramey, A. P. Shah, B. J. Sporer, N. M. Jordan, Y. Y. Lau, and R. M. Gilgenbach, *IEEE Trans. Plasma Sci.* **46**, 3928 (2018).
- ²N. R. Pereira and J. Davis, *J. Appl. Phys.* **64**, R1 (1988).
- ³D. D. Ryutov, M. S. Derzon, and M. K. Matzen, *Rev. Mod. Phys.* **72**, 167 (2000).
- ⁴J. L. Giuliani and R. J. Comisso, *IEEE Trans. Plasma Sci.* **43**, 2385 (2015).
- ⁵S. N. Bland, S. V. Lebedev, J. P. Chittenden, G. N. Hall, F. Suzuki-Vidal, D. J. Ampleford, S. C. Bott, J. B. A. Palmer, S. A. Pikuz, and T. A. Shelkovenko, *Phys. Plasmas* **14**, 056315 (2007).
- ⁶R. D. McBride, T. A. Shelkovenko, S. A. Pikuz, D. A. Hammer, J. B. Greenly, B. R. Kusse, J. D. Douglass, P. F. Knapp, K. S. Bell, I. C. Blesener, and D. A. Chalenski, *Phys. Plasmas* **16**, 012706 (2009).
- ⁷M. Krishnan, *IEEE Trans. Plasma Sci.* **40**, 3189 (2012).
- ⁸S. A. Pikuz, T. A. Shelkovenko, and D. A. Hammer, *Plasma Phys. Rep.* **41**, 291 (2015).
- ⁹S. A. Pikuz, T. A. Shelkovenko, and D. A. Hammer, *Plasma Phys. Rep.* **41**, 445 (2015).
- ¹⁰G. Sarkisov, S. Pikuz, T. Shelkovenko, and V. Romanova, in *1997 IEEE International Conference on Plasma Science* (IEEE, 1997), p. 177.
- ¹¹M. C. Mitchell, Ph.D. thesis, Cornell University, 2010.
- ¹²S. Bott, D. Haas, Y. Eshaq, U. Ueda, S. Lebedev, J. Chittenden, J. Palmer, S. Bland, G. Hall, D. Ampleford, and F. Beg, *IEEE Trans. Plasma Sci.* **36**, 2759 (2008).
- ¹³T. Pisarczyk, A. Rupasov, G. Sarkisov, and S. Shikanov, *J. Sov. Laser Res.* **11**, 1 (1990).
- ¹⁴S. N. Bland, D. J. Ampleford, S. C. Bott, A. Guite, G. N. Hall, S. M. Hardy, S. V. Lebedev, P. Shardlow, A. Harvey-Thompson, F. Suzuki, and K. H. Kwek, *Rev. Sci. Instrum.* **77**, 10E315 (2006).
- ¹⁵G. F. Swadling, S. V. Lebedev, G. N. Hall, S. Patankar, N. H. Stewart, R. A. Smith, A. J. Harvey-Thompson, G. C. Burdiak, P. de Grouchy, J. Skidmore, L. Suttle, F. Suzuki-Vidal, S. N. Bland, K. H. Kwek, L. Pickworth, M. Bennett, J. D. Hare, W. Rozmus, and J. Yuan, *Rev. Sci. Instrum.* **85**, 11E502 (2014).
- ¹⁶V. V. Ivanov, A. A. Anderson, D. Papp, B. R. Talbot, J. P. Chittenden, N. Niasse, and I. A. Begishev, *IEEE Trans. Plasma Sci.* **42**, 1153 (2014).
- ¹⁷V. V. Ivanov, A. A. Anderson, and D. Papp, *Matter Radiat. Extremes* **4**, 017401 (2019).
- ¹⁸W. Syed, Ph.D. thesis, Cornell University, 2010.
- ¹⁹W. Syed, R. B. van Dover, J. R. Petrie, M. D. Mitchell, and D. A. Hammer, *Appl. Phys. Lett.* **87**, 182505 (2005).
- ²⁰W. Syed, D. A. Hammer, M. Lipson, and R. B. van Dover, *AIP Conf. Proc.* **808**, 315 (2006).
- ²¹V. Ivanov, G. Sarkisov, P. Laca, V. Sotnikov, V. Kantsyrev, B. Jones, C. Coverdale, P. Lepell, C. Deeney, K. Struve, A. Astanovitskiy, D. Fedin, B. Le Galoudec, V. Nalajala, I. Shrestha, and T. Cowan, *IEEE Trans. Plasma Sci.* **34**, 2247 (2006).
- ²²A. Anderson, V. Ivanov, and D. Papp, *High Energy Density Phys.* **15**, 1 (2015).
- ²³R. M. Gilgenbach, M. R. Gomez, J. C. Zier, W. W. Tang, D. M. French, Y. Y. Lau, M. G. Mazarakis, M. E. Cuneo, M. D. Johnston, B. V. Oliver, T. A. Mehlhorn, A. A. Kim, and V. A. Sinebryukhov, *AIP Conf. Proc.* **1088**, 259 (2009).
- ²⁴M. R. Gomez, Ph.D. thesis, University of Michigan, 2010.
- ²⁵P. C. Campbell, J. M. Woolstrum, F. Antoulinakos, T. M. Jones, D. A. Yager-Elorriaga, S. M. Miller, N. M. Jordan, Y. Y. Lau, R. M. Gilgenbach, and R. D. McBride, *IEEE Trans. Plasma Sci.* **46**, 3973 (2018).
- ²⁶M. C. Jones, D. J. Ampleford, M. E. Cuneo, R. Hohlfelder, C. A. Jennings, D. W. Johnson, B. Jones, M. R. Lopez, J. MacArthur, J. A. Mills, T. Preston, G. A. Rochau, M. Savage, D. Spencer, D. B. Sinars, and J. L. Porter, *Rev. Sci. Instrum.* **85**, 083501 (2014).

²⁷S. M. Zakharov, G. V. Ivanenkov, A. A. Kolomenskij, S. A. Pikuz, A. I. Samokhin, and I. Ulshmid, *Pis. Zh. Tekhnicheskoy Fiz.* **8**, 1060 (1982).

²⁸I. H. Hutchinson, *Principles of Plasma Diagnostics* (Cambridge University Press, 2005).

²⁹I. H. Mitchell, J. M. Bayley, J. P. Chittenden, J. F. Worley, A. E. Dangor, M. G. Haines, and P. Choi, *Rev. Sci. Instrum.* **67**, 1533 (1996).

³⁰G. F. Swadling, S. V. Lebedev, N. Niasse, J. P. Chittenden, G. N. Hall, F. Suzuki-Vidal, G. Burdiak, A. J. Harvey-Thompson, S. N. Bland, P. De Grouchy, E. Khoory, L. Pickworth, J. Skidmore, and L. Suttle, *Phys. Plasmas* **20**, 022705 (2013).

³¹G. F. Swadling, Ph.D. thesis, Imperial College London, 2011.

³²J. D. Hare, J. MacDonald, S. N. Bland, J. Dranczewski, J. W. D. Halliday, S. V. Lebedev, L. G. Suttle, E. R. Tubman, and W. Rozmus, *Plasma Phys. Controlled Fusion* **61**, 085012 (2019).